Faraday Discussions

Accepted Manuscript

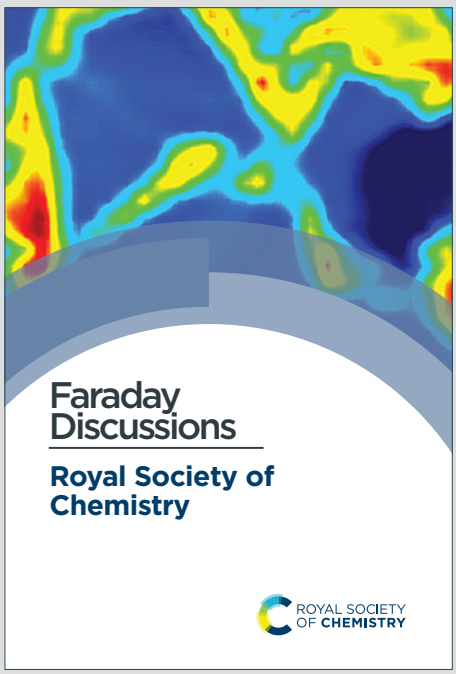

This article can be cited before page numbers have been issued, to do this please use: E. Winiewska, X. Shi, R. Newitt, V. Sanyal, K. Palanisamy and S. Menkin, *Faraday Discuss.*, 2026, DOI: 10.1039/D6FD00048G.

Faraday Discussions

View Article Online
DOI: 10.1039/D6FD00048G

PAPER

Role of Tin Seed Layers in SEI Evolution and Lithium Electrodeposition

Ewelina Wiśniewska[1,$ #], Xiaorui Shi[1, #], Rone Newitt[1], Ved Sanyal[2] , Krishnaveni Palanisamy[1,3], Svetlana Menkin[1,3*]

1. Yusuf Hamied Department of Chemistry, University of Cambridge, Lensfield Road, Cambridge, CB2 1EW, UK.

2. School of Chemistry, University of Edinburgh, Edinburgh, EH9 3FJ, UK.

3. The Faraday Institution, Quad One, Harwell Science and Innovation Campus, Didcot, OX11 ORA, UK.

* Corresponding author email: sm2383@cam.ac.uk

# Equal contribution.

$ presenting author

Received 00th January 20xx, Accepted 00th January 20xx
DOI: 10.1039/x0xx00000x

Metal batteries employing lithium or sodium anodes offer exceptional energy density but are limited by interfacial instability and uneven metal deposition, particularly in anode-free designs where lithium is plated onto a bare current collector. Here we demonstrate a rapid and scalable method for depositing tin seed layers on copper current collectors using a replacement reaction commonly employed in the electronics industry, enabling coating from aqueous solutions at room temperature. The resulting tin layer acts as an electronically conductive lithophilic seed that potentially improves solid–solid wetting between lithium and the current collector, promoting more uniform lithium electrodeposition in anode-free cells. The mechanistic roles of the tin seed layer and the solid–electrolyte interphase (SEI) are investigated through lithium–tin alloying and de-alloying processes combined with cyclic voltammetry (CV), scanning electron microscopy (SEM), X-ray diffraction (XRD), and scanning electrochemical microscopy (SECM). Here, we showed that the tin seed layer fundamentally alters the interfacial electrochemistry of copper, enabling faster charge transport across the SEI.

Introduction

The search for rechargeable batteries with higher energy density has led to a renaissance of interest in lithium (Li) metal anodes. However, potential safety issues due to Li dendrite growth and low Coulombic efficiency (CE) during cycling are delaying the practical implementation of lithium metal batteries (LMBs). Furthermore, the use of an excessively thick Li metal layer in complete battery cells reduces the practical volumetric energy density, increases material and production costs, and raises safety concerns in battery manufacturing.

"Anode-free" batteries (AFB), emerged as an attempt to overcome the challenges associated with LMBs. In an AFB configuration, the electrochemically refined Li metal anode is formed in situ by the reduction of Li ions originating from the cathode at the negative current collector during charging. Upon discharging, the plated Li metal is stripped out in the form of Li ions into the electrolyte and intercalated into the cathode. This configuration is intended to significantly reduce the amount of Li in the cell (often referred to as excess Li), which should result in higher volumetric energy density (approximately 400 Wh/kg and 1000 Wh/l compared to 250 Wh/kg, 600 Wh/l for LIBs, potentially produced on the same line).[1] Anode-free batteries hold the promise of a swift converting of today's batteries production lines into the production of anode-free batteries. However, the typical copper (Cu) current collector (CC) facilitates uneven and dendritic electrodeposition of Li. In particular, the lithiophobic nature of the Cu CC remains the biggest challenge.[1,2] Therefore, modification of the current collector surface has become another intensively investigated research direction.

Coating strategies generally fall into two categories based on their operating mechanisms: (1) ion-conducting inorganic layers that facilitate Li-ion transport across the metal–electrolyte interface and function as artificial solid–electrolyte interphases (SEI), and (2) electron-conducting metal or alloy coatings that reduce the Li nucleation barrier by improving Li–Cu solid–solid wetting.[3–5] Alloy-forming metals are particularly effective, as they enhance interfacial transport and promote uniform lithium nucleation and deposition.[6–9] Accordingly, lithiophilic layers based on metals such as zinc (Zn), aluminium (Al), silver (Ag), tin (Sn), magnesium (Mg) and indium (In), as well as pre-lithiated Li–Sn alloys, have been shown to significantly improve Li deposition behaviour and the performance of anode-free cells.[10,11] Among these materials, Sn is particularly attractive due to its strong alloying interaction with lithium and its ability to act as a conductive nucleation seed, making it a promising candidate for improving lithium deposition on Cu CCs.[12,13]

The evolving nature of the Cu surface and the inconsistent effects of Cu surface treatments have motivated the use of interfacial coatings to improve Li–Cu wetting and stabilise cycling in anode-free batteries (AFBs). However, such coatings add mass and volume, reducing energy density and highlighting the need for ultrathin and effective surface modifications. An important aspect on the practicality of AFBs is the stoichiometry or N/P ratio (defined as the capacity of the negative electrode to the positive electrode, that is the Li inventory of the cathode) when the lithophilic material contributes to capacity. The most desired scenario is when N/P<1 (ultimate goal N/P<<1) resulting in a two-stage process starting from (i) lithiation of the lithophilic coating and (ii) continued electrodeposition of Li metal on the fully lithiated phase. In this scenario, the amount of lithophilic coating is minimum to increase the capacity of the cell, however the typical problems associated with alloy anodes, such as pulverisation due to large volume changes and rapid degradation are expected to be minimal as well.[3] Thin or partially discontinuous coatings may act as nucleation seeds for lithium deposition, but their effectiveness still depends on interfacial kinetics, solid-solid wetting and charge transport at the interface. This work, rather than targeting a specific composition or thickness, aims to understand how Sn-based seed layers influence lithium electrodeposition. During the battery cycling, the layer may evolve through alloying and will therefore impact and interact with the SEI.

A practical route to deposit Sn on Cu is immersion (replacement) deposition,[14,15] which involves the transfer of electrons from a more electrochemically negative metal to a more positive metal according to reaction (1), resulting in the formation of a Sn coating on the Cu surface:

$$(1)\ 2\ Cu^0 + Sn^{2+} \rightarrow 2\ Cu^{+} + Sn^0$$

The standard electrode potentials of Cu and Sn differ by approximately 0.65 V (+ 0.51 V and – 0.14 V vs SHE respectively); therefore, to enable immersion Sn plating, ligands are typically introduced that form stronger complexes with Cu than with Sn. This effectively shifts the potential of Cu to around – 0.4 V vs SHE which makes it possible for the reaction to occur in room temperature. This process is widely used in the electronics industry to coat Cu current collectors on printed circuit boards, where the Sn layer protects Cu from corrosion and provides high surface wettability for soldering.[15] In such applications, the replacement deposition process is optimised to ensure surface coplanarity and prevent Cu exposure. Immersion Sn deposition is typically performed at temperatures between 10 and 80 °C with deposition times of 10–25 minutes, where lower temperatures produce thinner coatings (<1 µm) with finer grain structures.[16]

Improved performance of metal- or alloy-coated current collectors is commonly associated with reduced Li nucleation overpotential and enhanced cycling stability in half- and full-cell configurations.[17] A lower nucleation overpotential is generally interpreted as evidence of improved Li–substrate interfacial wetting and more favourable nucleation kinetics, which promote uniform Li deposition and suppress dendritic or mossy growth.[17,18] This behaviour often results in improved CE and extended cycling stability in Li||Cu half-cells, as well as enhanced capacity retention in anode-free full cells paired with conventional cathodes. For tin-based coatings, these effects are frequently attributed to the lithophilic nature of Sn and its ability to form Li–Sn alloys.[17] Density functional theory (DFT) calculations suggest that Sn-containing surfaces provide stronger Li adsorption and lower nucleation barriers compared with Cu, resulting in reduced Li–substrate interfacial energies and more favourable Li nucleation.[18] However, the reported reductions in nucleation overpotential are often relatively small and may fall within experimental variability, highlighting the need for complementary mechanistic studies that consider interfacial

transport and the evolution of the SEI. Consequently, the respective roles of the metal–collector interface and the evolving SEI in governing lithium nucleation and deposition remain insufficiently understood.

View Article Online
DOI: 10.1039/D6FD00048G

Here, we showed that nucleation overpotential is not the determining factor for Li metal anode cyclability; instead, long-term stability is controlled by interfacial transport processes and Li utilization. Consistently, the introduction of a pre-lithiated Sn interfacial layer, as opposed to metallic Sn, markedly improves cycling performance by promoting fast charge transport across the SEI and mitigating dead-Li formation.

Methods

Sn coating synthesis

Thiourea (1.83 g, 0.80 M, Sigma-Aldrich), sodium hypophosphite monohydrate (1.27 g, 0.40 M Thermo Fisher Scientific) and sodium citrate tribasic dihydrate (3.55g, 0.40 M, Sigma-Aldrich) were dissolved in 25 cm^3 of deionised water and then bubbled consistently with N_2 gas with stirring. In a separate flask, tin chloride (1.71g, 0.30 M, Thermo Fisher Scientific) was dissolved in 5 cm^3 of water and added dropwise to the first flask taking particular care to avoid formation of a sticky white precipitate. During use this flask was continuously bubbled with N_2 or stored sealed with Parafilm to prevent insoluble tin oxide formation.
Two methods of applying the coating to one side of Cu foils were used. Firstly, 2 cm^2 Cu foils were placed on Viton O-rings and the bath solution was added dropwise on top of the foil to completely cover the surface. Secondly, a Viton O-ring was placed on a corrosion resistant pedestal and filled with the bath solution until it formed a bubble held by surface tension above the top of the O-ring. The Cu foil was then placed face down such that it was floating on the bubble but not touching the O-ring allowing the entire surface to be coated evenly. After the samples were coated, they were washed with water (four rinses of 10 ml each), dried under N_2, washed with acetone (two rinses of 10 ml each) and dried with N_2 again before being dried in a vacuum oven at 60°C overnight. In practice the second method was more reliable for preparing samples and was used for the majority of samples. Deposition time refers to how long the Cu foil was floated on the deposition solution surface. In this manuscript the Sn deposited Cu samples are termed Sn@Cu.

Coin Cell assembly

Cell assembly and air-sensitive material handling were done in an argon glovebox (MBraun, O_2, H_2O < 0.1 ppm). The electrolytes used were the following: 1 M LiPF6 (Sigma) in ethylene carbonate and ethyl methyl carbonate (EC: EMC 3:7 volume ratio) termed LP57 in this study. Lithium metal disks (15.6mm x 0.25mm thick) were purchased from PI-KEM, opened, and stored in an argon glovebox, used as received. Stainless steel 316-coin cell parts (Cambridge Energy) were sonicated in ethanol: acetone 1:1 mix and dried at 60°C under vacuum overnight prior to cells assembly. Celgard 3501 (polyethylene – polypropylene layered) separator was used after being dried in vacuum at RT. Coin cells consist of two bases, a spring, three 0.49mm stainless steel disks, an Li electrode, and a Celgard separator with 75 µL LP57 electrolyte, respectively.

Chemical Pre-Lithiation

Chemical pre-lithiation and air sensitive material handling was done in an argon glovebox (MBraun, O2, H2O < 0.1 ppm). Coin cells were assembled with a spring, four 0.49 mm stainless steel disks, a Li electrode and a Sn@Cu foil such that the Sn coated face and Li metal were shorted (importantly, without a separator). 75 µL of LP57 was used and the coin cells sealed overnight. These cells were then disassembled and the pre-lithiated Sn@Cu foil removed and inserted into a cell for cycling.

Coin Cell Cycling

Assembled coin cells were rested at OCP for 24 hours and then cycled (Ivium Ivicycle C030) using a constant current protocol. Limitations were set for maximum durations and, during discharge, cutoff voltages to prevent undesired processes (such as Cu oxidation and corrosion) which was set at 3.00 V as a safety limit unless otherwise specified. The half-cell orientation was chosen so that the negative current process always corresponded to charging and the positive current process always to discharging.

SEM & EDX

The surface morphology of the tin-coated copper foils was examined using scanning electron microscopy (SEM) (Tescan Clara-2) in secondary electron imaging mode (E–T detector). Measurements were performed at an accelerating voltage of 3 keV, with a working distance of ~10 mm and a beam current of 43-44 pA. The samples were transferred into the microscope using a sealed transfer module to minimise exposure to ambient atmosphere prior to imaging. Images were acquired in conventional scanning mode with a field of view of 50 µm (Sn@Cu samples) or 100 µm (Li on Sn @Cu samples). No additional conductive coating was applied prior to imaging. EDX analysis was performed using the same machine with an accelerating voltage of 3 keV, a working distance of ~10 mm and a beam current of 300 pA.

View Article Online
DOI: 10.1039/D6FD00048G

CV

A three-electrode PEEK cell was used for cyclic voltammetry measurements. Li metal (0.4 × 1.4 cm², PI-KEM), Sn@Cu (0.5 × 0.6 cm²), and a Ag wire were used as the counter electrode, working electrode, and reference electrode, respectively. The Li metal and Sn@Cu electrodes were positioned facing each other in the cell assembly. G (Whatman) lass fiber B was used as the separator, and an excess amount of LP57 electrolyte was added during cell assembly.

SECM

Approach curves and SECM maps of Cu and Sn/Cu electrodes were recorded in feedback mode in an electrolyte containing 5 mM ferrocene (Fc) in 1 M LP57. The Sn@Cu electrode was prepared with a deposition time of approximately 1 h. A Pt ultramicroelectrode (UME, r = 5 µm) served as the SECM tip (working electrode), while Li metal was used as both the reference and counter electrodes. All measurements were performed using a CH Instruments 900-series electrochemical workstation specifically designed for SECM (CHI920D, USA). The potential of the Pt UME was held at 3.6 V vs. Li^+/Li metal to oxidize the redox mediator.

Approach curves were analysed using the theoretical model developed by Cornut and Lefrou for both insulating and conductive substrates.[19] The fitting procedure was carried out using the MIRA software package (version 3.1, G. Wittstock, University of Oldenburg, Germany).

Results and Discussion

Results

1. Sn coating optimisation

Sn metal was deposited on Cu foils via immersion tin plating using a modified procedure adapted from the printed circuit board (PCB) industry. The method involves introducing thiourea to complex copper, thereby reducing the effective reduction potential of Cu and enabling spontaneous reduction of Sn^{2+}. The procedure was optimised for single-sided coatings on 2 cm² Cu foils, suitable for experiments in coin cells and SECM. While standard immersion tin coating of Cu current collectors in circuit boards is typically performed at 80 °C with full immersion of the Cu component, here Sn was deposited by either applying a drop of the deposition solution onto the copper surface or floating the Cu foil on the solution at 25 °C. This room-temperature deposition approach limits the amount of Sn deposited, ensuring that excessive Sn does not accumulate on the substrate, which would otherwise accelerate anode degradation and reduce the achievable energy density of the cell.

To investigate the effects of deposition time, coatings prepared for 10 minutes and 1 hour were compared. XRD spectra of the tin-coated copper foils for 10 min (Fig. 1a) and 1 h (Fig. 1b) deposition times show peaks characteristic of copper (Cu (111), Cu (200), Cu (220), 100:58:19), together with a small peak at 30.1° assigned to Cu_6Sn_5 (101). This observation is consistent with studies of immersion-tin coatings used in PCB manufacturing where a Cu_6Sn_5 intermetallic layer forms at the Cu/Sn interface during the early stages of deposition and can be detected by XRD. In the 1 h coating, a very small peak appears at 30.6°; we have assigned this to the Sn (200) reflection - as metallic tin is expected to deposit on the intermetallic compound – although, its low intensity could alternatively be attributed to the η'-Cu_6Sn_5 phase, which has a reflection near 30.5°, or a measurement artefact. Peak assignments were made using ICDD PDF 04-0836 for Cu (fcc) and ICDD PDF 04-0673 for metallic tin (β-Sn, tetragonal)).[20,21]

The overall low intensity of the Sn and intermetallic peaks suggests a very thin coating (<1 µm) forming during deposition at ambient temperature. However, the 1-hour sample shows significantly more pronounced Sn-related peaks compared to the 10-minute sample (Fig. 1). This suggests that surface roughness allows Cu to remain accessible for the replacement reaction until a complete Cu_6Sn_5 layer is established. Similar behaviour is reported in conventional immersion-tin processes at elevated temperatures (~80°C), where after formation of the intermetallic layer, Sn metal begins plating after no surface accessible Cu remains.[21] These findings are supported by EDX analysis (Fig. S2-S3, Table S2), which shows the atomic Cu:Sn ratio shifting from 65:35 after 10 minutes to 53:47 after 1 hour, confirming progressive tin enrichment. The peak assignment of Cu_6Sn_5 in the 10 min sample is made based from the literature despite the Sn concentration being too low in the EDX. It is likely that the coating does have the correct ratio of Cu:Sn but is thin enough at 10 minutes that the EDX penetrates through the layer and sees the bulk Cu underneath.

View Article Online
DOI: 10.1039/D6FD00048G

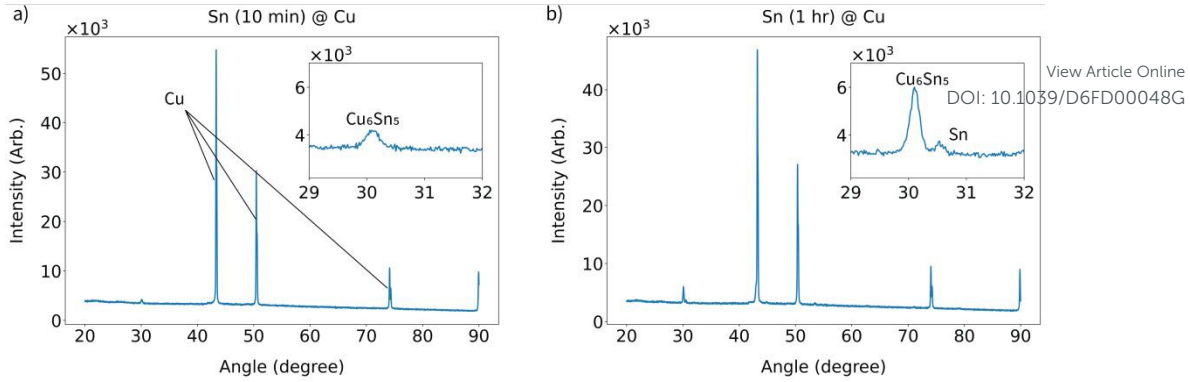

Figure 1 XRD analysis of copper coated with tin: (a) Sn@Cu with Sn deposited for 10 min and (b) Sn@Cu with Sn deposited for 1 h.

SEM images of the 10 min (Fig. 2a) and 1-hour (Fig. 2b) Sn coatings reveal a conformal layer on the relatively rough copper substrate. The longer deposition time promotes the growth of cube-shaped Sn crystallites, consistent with increased metallic Sn deposition observed by XRD and EDX, which shows atomic ratios of 65:35 (Cu:Sn) for the 10-minute sample and 5:95 (Cu:Sn) for the grains observed (see Table S2 in the Supporting Information, Figs. 1 and S2-S3). EDX analysis also shows that the brighter regions in the SEM images correspond to areas with higher Sn concentration. These bright regions are larger and more pronounced in the 1-hour coating, which may be attributed to a higher metallic Sn content and the consequent formation of Sn oxide, contributing to increased sample charging during SEM imaging.

Another 1-hour coating sample was stored for two months to allow additional time for Cu diffusion to occur. EDX analysis of the bulk surface in both the fresh and aged samples shows compositions consistent with Cu_6Sn_5, with Sn contents of for the fresh and aged samples, respectively (Table S2). This indicates that Cu_6Sn layer grows over time. Metallic Sn is still observed on the surface of the aged sample, with particles of approximately similar size to those in the fresh sample, suggesting that Cu diffusion over the two-month period has not yet reached the surface (Fig S3). However, the diffusion of Cu during storage potentially grows the active Sn-Cu alloy layer on Cu.

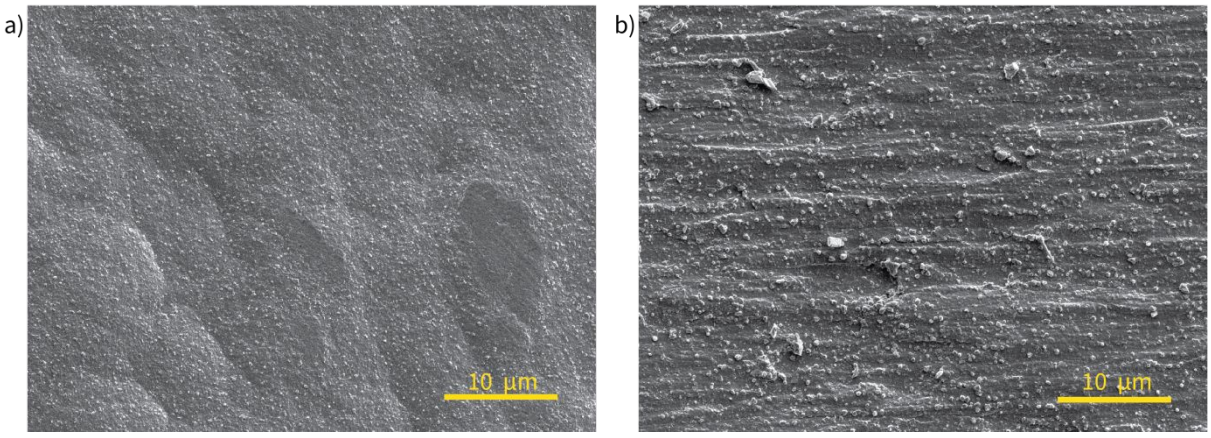

Figure 2 SEM images of (a) a 10 min Sn@Cu coating and (b) a 1-hour Sn@Cu coating.

2. Tin lithiation and Li electrodeposition fundamentals

To examine the influence of the tin coating on lithium deposition morphology, SEM images were obtained. Fig. 3 shows the surface morphology of the current collectors after 2.5 cycles, at the end of the plating process. Dendritic Li deposition is observed on the Cu current

collector, whereas the Sn@Cu current collector exhibits a more uniform, flatter, leaf-like Li morphology. This demonstrates that the Sn coating can facilitate more even and non-dendritic Li deposition.

View Article Online
DOI: 10.1039/D6FD00048G

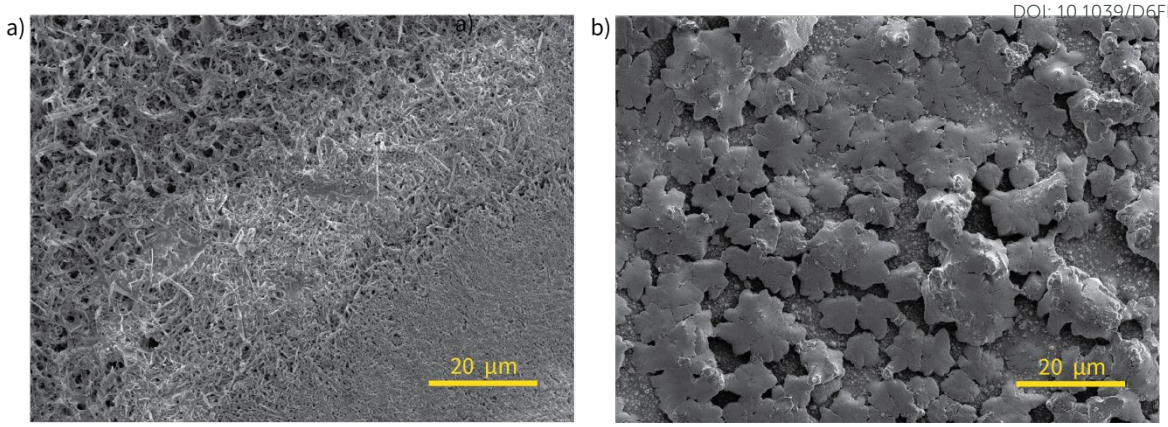

Figure 3. Surface morphology of Sn@Cu current collectors after plating following 2.5 cycles. Images correspond to Cu Li (a) and 1 h Sn@Cu Li (b) cells, respectively. The cells were cycled at a current density of 0.5 mA cm^{-2} with a capacity of 0.5 mAh cm^{-2}. The voltage window for cycling was –0.5 V to 3 V.

To demonstrate the electrochemical activity of the Sn@Cu current collectors, CV measurements were performed (Fig. 4). The CV profiles show the formation of Sn–Li alloys, indicated by a shoulder at approximately 0.5 V and a broad peak between 0.35 and 0 V vs. Li^+/Li (Fig. 4a). Typical dealloying peaks appear at 0.6–0.8 V vs. Li^+/Li during the reverse scan. Sn re-oxidation and Li_2O formation peaks were observed at 1 V.[22] With continuous cycling, the Sn–Li alloying and dealloying peaks gradually diminish, while a characteristic Cu oxide reduction peak appears at approximately 1.4 V, which may indicate degradation of the Sn layer and exposure of the underlying Cu substrate (Fig. S4). [23]

When the reduction scan was extended into the negative potential range (down to −0.5 V vs. Li), the alloying peak transitioned into Li deposition (Fig. 4b), as evidenced by the characteristic current cross-over at approximately −0.1 V. In the subsequent anodic scan, a very broad oxidation peak centred around 1.4 V was observed and assigned to Sn de-alloying, Li stripping, Sn and Cu re-oxidation. The higher stripping overpotential of Li from the Sn seed layer is potentially due to slower Li diffusion in the Li–Sn alloy (Fig.4b and S4). A repeat of the CV experiment resulted in a similar peak, this time the stripping and de-alloying were resolved (Fig. S4c-d). With increasing cycle number, the intensity of the plating and stripping peaks decreases, while the overpotential increases, consistent with previous literature reports.[24]

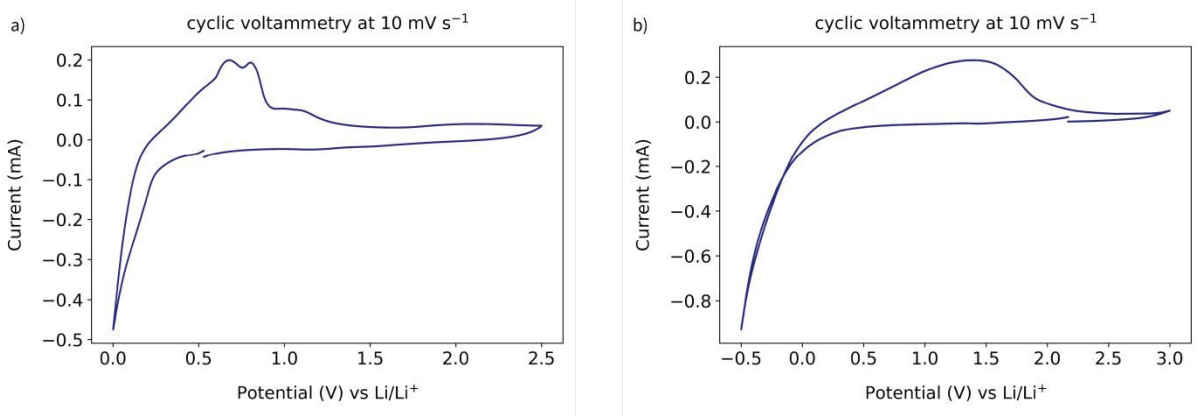

Figure 4 Cyclic voltammetry at a scan rate of 10 mV s^{-1} in a three-electrode configuration. WE: 1-hour Sn @Cu, RE: Ag wire, CE: Li metal; scan range OCV to 0 V **(a)** OCV to −0.5 V **(b).**

The Sn@Cu samples were tested in two-electrode coin cells via galvanostatic cycling, the resulting voltage profile is shown in Fig. 5. The profile can be divided into four main parts: SEI formation, oxide reduction and alloying (1- blue), Li plating (2- green), Li stripping (3-pink), and de-alloying (4- yellow).

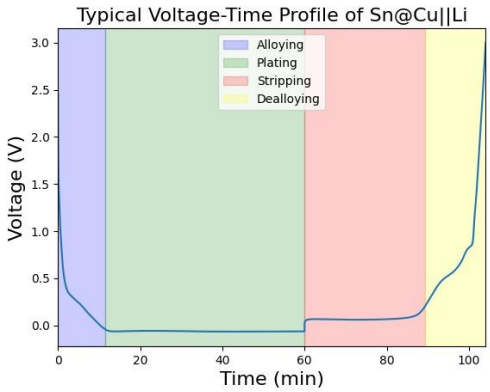

View Article Online
DOI: 10.1039/D6FD00048G

Figure 5 Typical voltage profile of a Sn@Cu||Li cell cycled at 0.5 mA cm^{-2} with a capacity of 0.5 mAh cm^{-2}. The voltage profile shown corresponds to a 1-hour Sn@Cu electrode at cycle 10. The alloying, plating, stripping and dealloying regions are highlighted by blue, green, red and yellow shading, respectively.

The physical interpretation of the voltage trace in the Sn–Li system is well established. The first, sloping part of the lithiation voltage trace is typical for lithium alloy anodes, while the second part is characteristic of lithium electrodeposition in lithium metal batteries.[25–29] The lithiation of a Sn alloy anode consists of three parts: SEI formation, Sn oxide reduction and Sn/Sn–alloy lithiation. During the first charge, tin lithiation occurs after SEI formation and Sn oxide reduction, and is followed by Li plating. In principle, SEI formation should not occur in subsequent cycles; however, due to the large volume changes associated with both tin alloy lithiation and Li electrodeposition, repeated breakdown and repair of the SEI takes place. When the potential of the Sn@Cu||Li half-cell is driven to negative potentials, a square-like voltage trace corresponds to Li metal electrodeposition. During stripping, the order of these processes is reversed: Li is first stripped (resulting in the square-like shape of the voltage curve), followed by the typical de-lithiation profile of the Sn alloy. This behaviour of the voltage curves is consistent across all experiments. The ratio between the sloping (alloying) region and the plateau (plating) region corresponds to the ratio of the lithium used for tin lithiation to that used for lithium metal plating. Ideally, this ratio should be minimized, meaning Sn/Li << 1.

Although the overpotential measured in half-cells is a useful parameter for investigating metal anodes, it has several significant limitations. The measured overpotential during charge is the sum of multiple contributions, including solution resistance (η_{IR}), charge-transfer and Li nucleation resistance (i.e., activation overpotential, η_{ac}), desolvation of Li^+ ions (η_{desolv}), alloying reactions (η_{alloy}), tin oxide reduction, and SEI formation(η_{SEI}). Thus, the total overpotential can be expressed as Eq. 1:

$$(1) \quad \eta_{total} = \eta_{IR} + \eta_{ac} + \eta_{desolv} + \eta_{alloy} + \eta_{SEI}$$

To deconvolute the voltage profiles during cycling of the Sn@Cu electrode, we assumed that the bulk electrolyte resistance, Li^+ desolvation, and ion transport across the SEI remain unchanged regardless of whether Sn alloying/dealloying or Li plating/stripping is the dominant electrochemical process. Hence, η_{IR} , η_{desolv} and η_{SEI} remain constant during cycling. Under this assumption, the total overpotential can be expressed as the sum of the overpotentials associated with Li plating/stripping and Sn alloying/dealloying.

3. Chronopotentiometry – voltage trace analysis

The lithiation of Sn and Sn–Cu alloys, followed by sequential Li electrodeposition, was studied in Sn@Cu||Li coin cells. Galvanostatic plating and stripping cycles were performed at a current density of 0.5 mA cm^{-2} with a capacity of 0.5 mAh cm^{-2} in 1 M $LiPF_6$ in EC: EMC (3:7) electrolyte (commonly referred to as LP57). Fig. 6 illustrates prolonged cycling, with selected regions magnified, whereas Fig 7a shows the corresponding voltage profiles at cycles 2, 40, and 80 overlaid for comparison. The sloping voltage profile at the start of charging confirms that the Sn-containing surface first alloys with lithium prior to lithium metal deposition.[22,30]

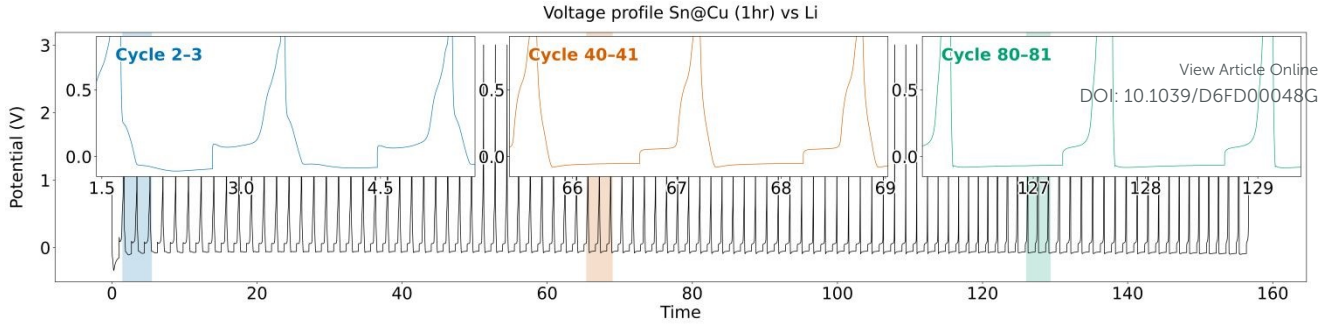

View Article Online
DOI: 10.1039/D6FD00048G

Figure 6 Voltage profiles for 1-hour Sn@Cu ||Li cell. The cell was cycled at 0.5 mA cm^{-2} for 100 cycles, with charging and discharging capacity being 0.5mAh cm^{-2}. The insets present zoomed-in voltage profiles corresponding to cycles 2–4 (blue), 38–40 (orange), and 80–82 (green).

Fig. 7a highlights the evolution of the alloying/dealloying and plating/stripping processes as the cycling progress. At the beginning of cycling (cycle 2), SEI formation begins at relatively high voltages, as indicated by the deviation of the voltage profile from the vertical line, while alloying occurs at approximately 0.25 V, lower than the theoretical value but consistent with the CV result. As cycling proceeds (cycle 40), the alloying feature remains evident prior to Li plating. However, the voltage profile deviates more strongly from the vertical line, starting at around 1 V, likely due to the combined effects of lithiation and SEI formation. Towards the end of cycling (cycle 80), the alloying feature becomes much less pronounced, with the electrochemical behaviour appearing to be dominated by Li plating and stripping. During discharge, the gradual voltage increase following the Li stripping plateau corresponds to the dealloying of the Sn coating (Fig.7a). The dealloying process consistently terminates at approximately 0.8 V, regardless of cycle number, consistently with the CV measurements (Fig. 4). Both the Li stripping and Sn dealloying capacities decrease with continued cycling, indicating progressive degradation (Fig 7a).

The voltage profiles at cycle 10 for three different Sn-coated samples are compared in Fig. 7b. The 10 min sample exhibits a significantly lower alloying-to-plating and dealloying-to-stripping ratio than the 1-hour sample. This suggests that the Sn replacement reaction is incomplete after 10 minutes. The longer coating times lead to the formation of a thicker, or more tin based, Sn@Cu layer, consistent with the XRD and EDX results, leading to more extensive Li–Sn alloying prior to lithium plating. In addition, we tested the effect of storage of the Sn@Cu samples (aged Sn@Cu) on their electrochemical performance. The 1-hour aged Sn–Cu sample exhibited significantly higher SEI formation, lithiation, and de-lithiation capacities in cycle 10.

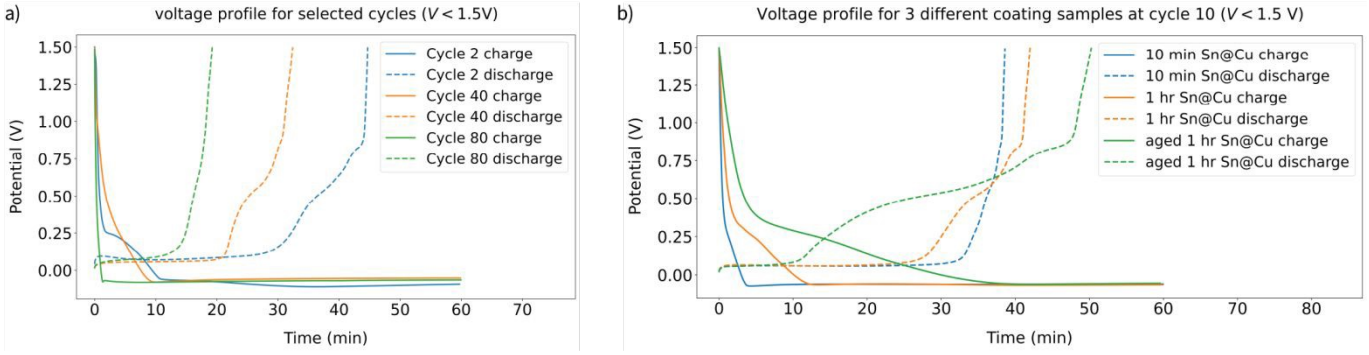

Figure 7 Voltage profiles for cells cycled at 0.5 mA cm^{-2} with a capacity of 0.5 mAh cm^{-2}. The solid lines represent the charge process, while the dashed lines represent the discharge process. **a)** Cycle number 2, 40 and 80 for 1-hour Sn @Cu||Li cell. **b)** Cycle number 10 for 10-min Sn@Cu||Li (blue), Sn (1 h)@Cu||Li (orange), Sn (1 h coating - 2 month old)@Cu||Li (green) cells.

Coulombic efficiency (CE) and stripping capacity were plotted to compare the cycling performance of Sn@Cu with different coating/aging time. As shown in Fig. 8, cycling of the Sn@Cu||Li half-cells resulted in a rapid decrease in both stripping capacity and CE for all samples. Since the cycling is conducted in half cells, where a large reservoir of Li is present, the trends of the stripping capacity are the same as the trends of CE. Notably, the sample with shorter Sn coating time exhibited lower initial capacity and CE; however, it showed a similar degradation rate to the 1-hour coating samples during the first 30 cycles. The 1-hour Sn@Cu sample that was stored for a longer period displayed a higher initial capacity but experienced faster degradation. Interestingly, after approximately 40 cycles, the aged Sn@Cu sample exhibited an opposite trend in stripping capacity and CE, with a sharp decrease

followed by a similarly sharp increase, while the 'fresh' samples—both the 10-min and 1-hour Sn–Cu—exhibited two distinct peaks in stripping capacity and CE.

View Article Online
DOI: 10.1039/D6FD00048G

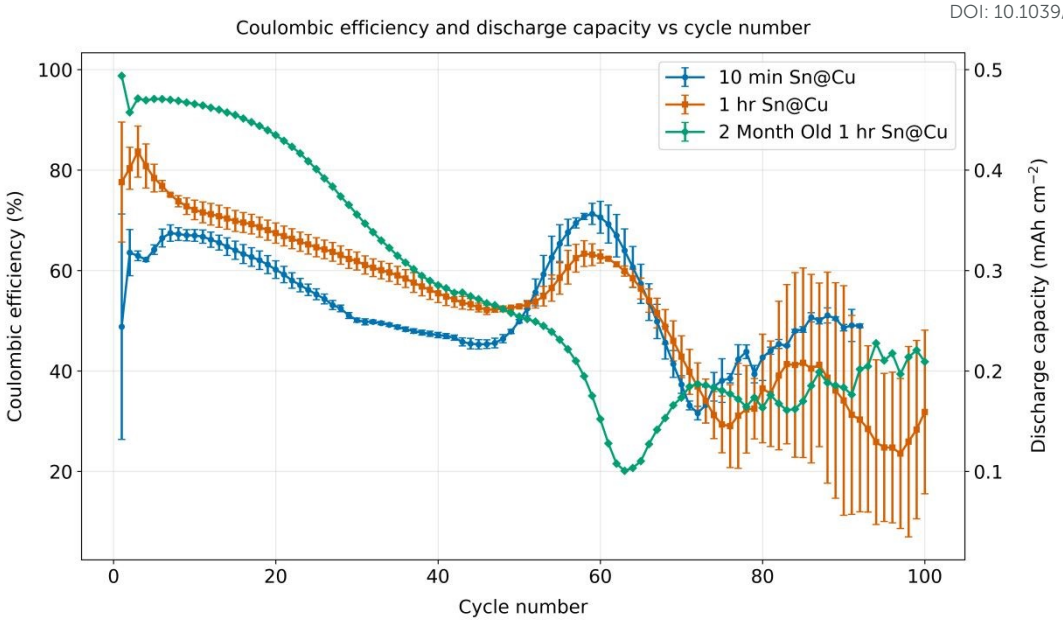

Figure 8 The coulombic efficiencies and discharge capacities of a fresh 10-min deposition time Sn@Cu||Li sample (blue), a fresh 1-hour Sn@Cu||Li sample (Orange) and a aged 1-hour Sn@Cu||Li sample which has been stored for two months before assembly into a coin cell (green). Error bars indicate the distribution between the tested cells.

To better understand the oscillations in CE (Fig. 8), the alloying/plating and dealloying/stripping capacities were separated (Fig.9). Based on the typical cycling stage assignment highlighted in Fig 5, the alloying stage was approximately defined as the processes occurring from the beginning of charging to the onset of the voltage plateau, while the plating stage corresponds to the voltage plateau in the negative voltage. During discharge, the stripping stage was defined as the region from the onset of discharge to the end of the voltage plateau, whereas the dealloying stage corresponds to the subsequent sloping increase in voltage. A full description of the transition point assignment and details of voltage plateau calculation can be found in the SI and Figs. S5-8. Comparison of the capacity magnitudes as a function of cycle number (Fig. 9 and Figs. S7) shows that when the dealloying contribution is significant, both capacity and efficiency decrease. In contrast, when the dealloying contribution is negligible around cycle 60, the capacity increases. In this case, the local maximum is followed by oscillations in the available capacity, which can be attributed to parasitic reactions at the end-of-life of the sample beyond cycle 70. The apparent increase in dealloying capacity beyond this point, when the alloying capacity is nearly zero, arises from the analysis code not terminating the integration at voltages above ~0.8 V, leading to an artificially inflated dealloying capacity (Fig. S6). This artifact only appears when the dealloying voltage profile slope becomes negligible (i.e., after cycle 80).

As the alloying capacity decreases, the corresponding dealloying capacity also diminishes, and a larger fraction of the charge is instead used for Li plating and stripping. Consequently, the electrochemical behaviour gradually transitions from alloying-governed processes to predominantly lithium plating and stripping, suggesting progressive loss of electrochemically accessible Sn during cycling.

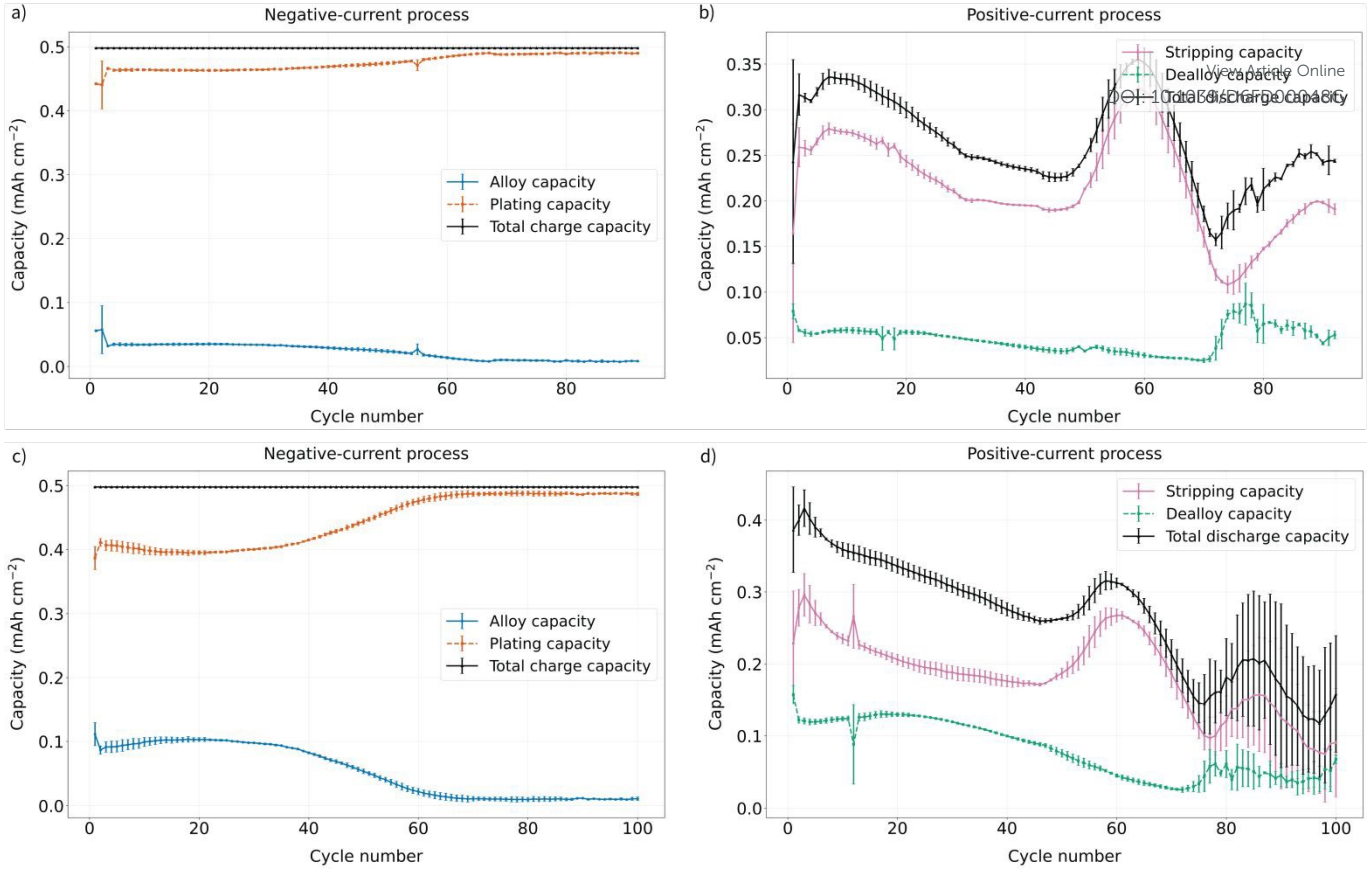

Figure 9 Deconvolution of cycling capacities of Sn@Cu||Li cells cycled at 0.5 mA cm^{-2} with a capacity of 0.5 mAh cm^{-2} and an upper cutoff voltage limited to 3 V. Deconvolution of alloying and plating: **(a)** 10 min Sn@Cu **(c)** 1 h Sn@Cu with. Dealloying and stripping: **(b)** 10 min Sn@Cu **(d)** 1 h Sn@Cu.

4. Optimizing the cycling procedure

To limit the Sn alloy-related degradation, such as Sn seed layer cracking (Fig. 10b), it is essential to minimise the extent of dealloying and operate the cell primarily through Li plating and stripping. To reduce the dealloying capacity, lower cut-off voltages were chosen.

As shown in Fig. 10, by the end of the stripping process in the first cycle, a large amount of leaf-like lithium remains on the surface of the bare Cu CC (Fig. 10a). In contrast, significantly less Li is observed on the surface of the 1 h Sn@Cu CC (Fig. 10b), indicating that the Sn coating reduces dead Li formation and promotes more complete Li stripping. The cracking observed in the Sn coating is likely induced by the substantial volume changes associated with Sn alloying and dealloying. Discharge voltage limited samples resulted in significantly more

homogeneous Sn alloy surface, no evidence of dead Li was observed on the stripped samples (Fig. 10c-e) consistent with the improved cyclability and CE.

View Article Online
DOI: 10.1039/D5FD00048G

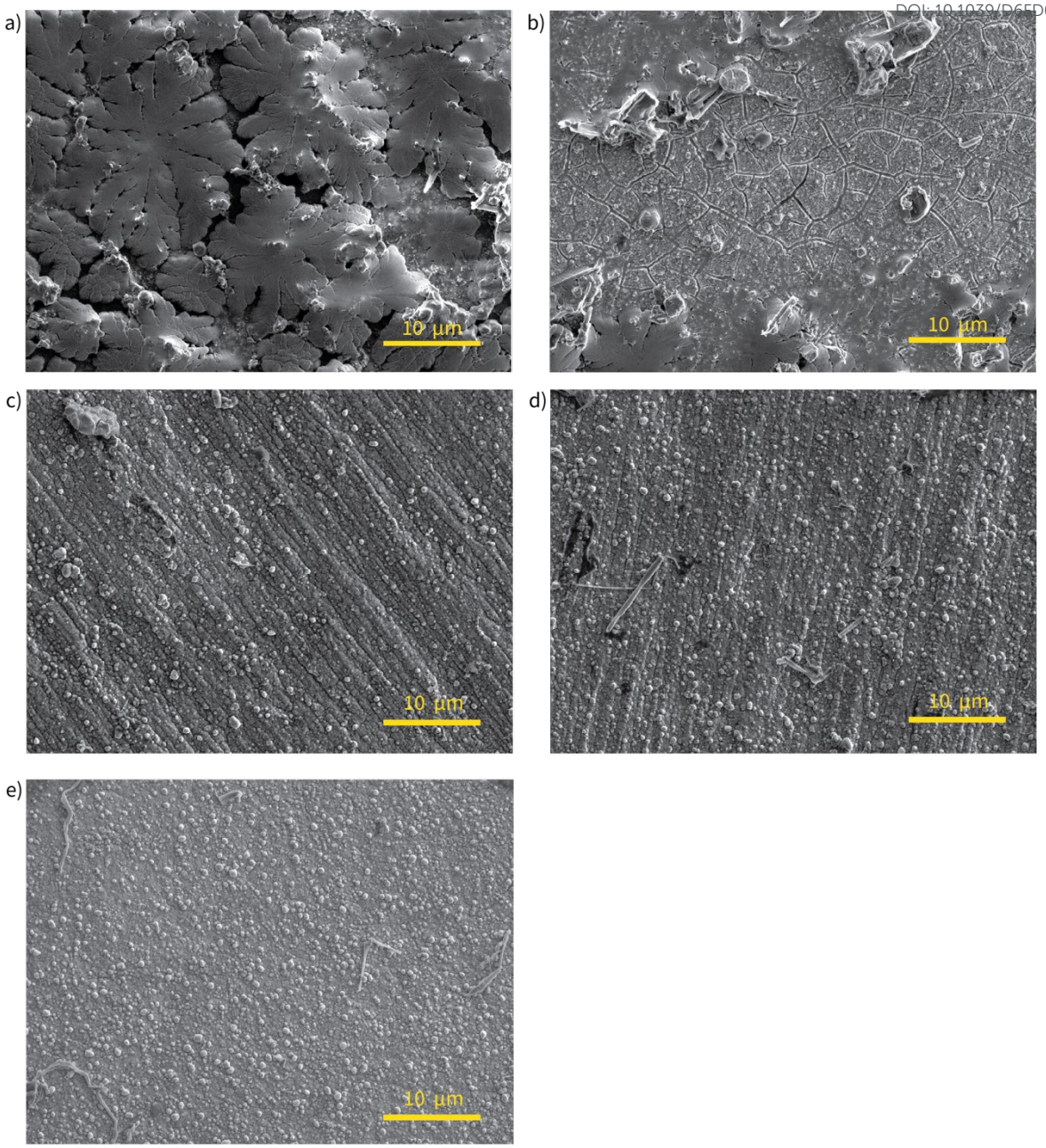

Figure 10 Surface morphology of Sn@Cu current collectors after stripping following a single cycle. Images correspond to Cu Li (a) and 1-hour Sn@Cu Li (b-d) cells. The cells were cycled at a current density of 0.5 mA cm^{-2} with a capacity of 0.5 mAh cm^{-2}. The voltage window for cycling was –0.5 V to 3 V (b), 0.17 V (c), 0.45 V (d) and 0.57 V (e), respectively.

Fig. 11 shows the CEs and capacities as a function of cycle number for cells cycled with different discharge cut-off voltages. Before analysing the degradation trends, it is important to note that while the signature of alloying is observed in all the voltage profiles until cycle 40 in the cell with the 3V cutoff, significant evidence of alloying appeared only in the first cycle in cells in which the dealloying was restricted, as expected (Fig. S10). This indicates that limiting the cutoff voltage effectively suppresses repeated alloying and dealloying, thereby reducing degradation of the Sn layer.

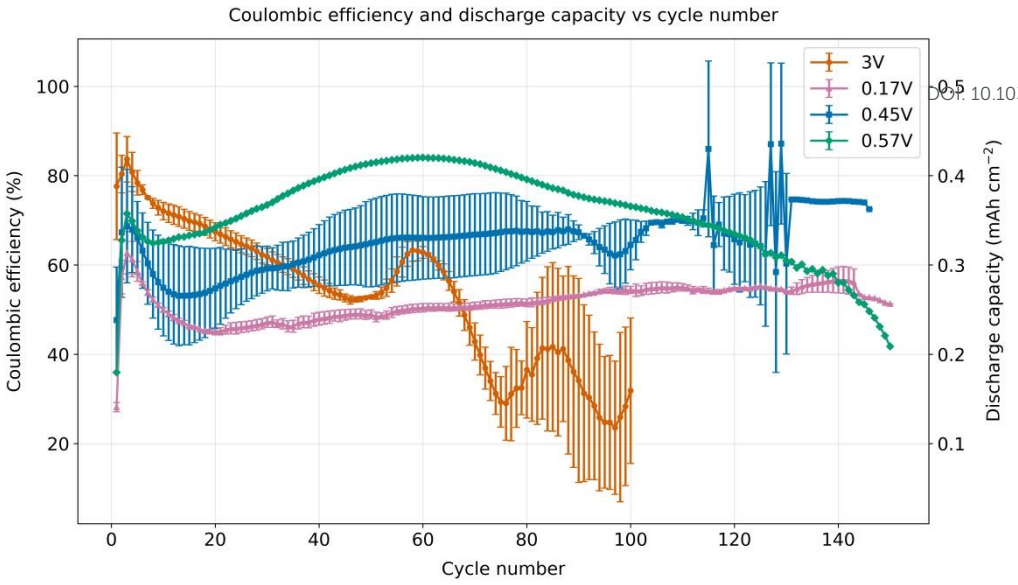

Figure 11 CE and stripping capacity as a function of cycle number under different upper cut-off voltages: 3 V (orange), 0.17 V (pink), 0.45 V (blue), and 0.57 V (green). Cells were cycled at 0.5 mA cm^{-2} with a charge/discharge capacity of 0.5 mAh cm^{-2}.

When the discharge cutoff voltage is limited, the discharge capacity primarily originates from Li stripping. During the initial cycles, a large fraction of the charge is consumed by SEI formation, Sn oxide reduction, and alloying reactions, resulting in a significantly lower discharge capacity (Fig. 8, 9, 11). The discharge capacity decreases with the cutoff voltage from 3 V to 0.17 V (Fig. 11). After the fourth cycle the capacity of all the tested samples sharply decrease. In the 3 V sample, this decrease continues until approximately cycle 50, followed by discharge capacity and CE fluctuation, which were attributed to the transition from alloying-governed process to predominantly Li plating and stripping (Fig. 11).

Similar to the samples cycled with a cutoff voltage of 3 V, the discharge capacity with more limited cut-off voltage initially increases after several cycles and subsequently drops abruptly, which may be attributed to the degradation of the formed Li anode (Fig. 11). From cycle 10 onward, a markedly different trend is observed for the samples with limiting cutoff voltages. For these samples, both the discharge capacity and the CE increase between cycle 10 and approximately cycle 140 for the 0.45 V and 0.17 V, and until about cycle 60 for the 0.57 V. Notably, the sample with a cutoff voltage of 0.57 V exhibits the highest maximum discharge capacity. However, this maximum is reached only after approximately 60 cycles, after which the capacity degrades at a similar rate over the subsequent 60 cycles. The capacity–cycle number trends for the 0.17 V and 0.45 V cutoff voltages are quite similar.

The magnitude of the error bars reflects the cell-to-cell variability. The relatively small error bars observed for the 0.17 V cutoff sample in the later cycles indicate more stable interfacial behaviour. In contrast, the larger error bars observed for the 3 V cutoff sample suggest the occurrence of underpotential Cu stripping at 3 V, which promotes Cu plating and leads to pronounced cycling instability.

5. Chemical pre-lithiation

Chemical pre-lithiation of the Sn@Cu samples was achieved by maintaining physical contact with Li metal in the presence of a Li-ion-conducting electrolyte (LP57). Notably, the cells were assembled without a separator, enabling the spontaneous formation of the Sn–Li alloy.

Cycling of the pre-lithiated cells with limited discharge voltages (Fig. 12) showed trends similar to those observed for the non-pre-lithiated cells (Fig. 11), but clear differences are observed in the early cycles. The pre-lithiated cells exhibited comparable discharge capacities during the initial cycles, as well as similar rates of capacity increase. Despite this, their cycle life differed more significantly, which may reflect cell-

to-cell variability associated with coin-cell assembly. Notably, the cell limited to 0.57 V delivered a slightly higher capacity, as expected for the highest discharge-voltage cutoff.

View Article Online
DOI: 10.1039/D6FD00048G

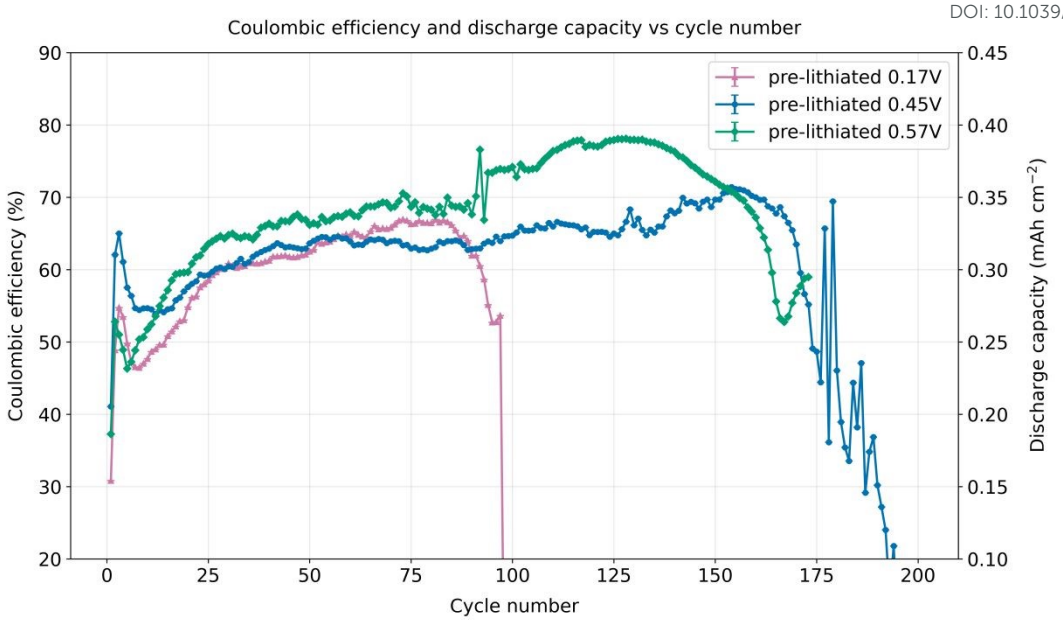

Figure 12 CE and stripping capacity as a function of cycle number under different upper cut-off voltages: 0.17 V (pink), 0.45 V (blue), and 0.57 V (green).

To compare the influence the chosen cut-off voltage, the cycling behaviour shown in Fig. 11 and 12 can be contrasted. At the lowest voltage limit (0.17 V), the pre-lithiated samples had a much higher discharge capacity than the non-pre-lithiated after the initial cycles. The trend lasted until around cycle 90, after which the performance of the pre-lithiated cell plummeted. At the intermediate limit (0.45 V), the discharge capacity was consistently slightly higher for the pre-lithiated sample, with both samples performing with around 60-70% CE. Lastly, at the 0.57 V limit, the discharge capacity was higher for the non-pre-lithiated sample. This behaviour changed beyond cycle 100, with the pre-lithiated sample outperforming the non-pre-lithiated.

Upon charging the pre-lithiated Sn@Cu half-cells, a different voltage profile was observed (Fig. 13), with no pronounced alloying signature detected during the first charge. The voltage profile during the first cycle of the pre-lithiated samples differs markedly from that of the non-lithiated Sn@Cu electrodes. While the latter exhibits a distinct feature associated with Sn–Li alloy formation, the former show a profile resembling Li plating on Cu. Specifically, the profile initially displays a locally most negative peak (here referred to as the nucleation overpotential), commonly attributed to Li nucleation, followed by a local minimum associated with subsequent surface area growth (Figs. 13 and S10). Notably, the nucleation overpotential in the first cycle of the pre-lithiated electrodes is generally larger than that of the non-lithiated samples and shows significant cell-to-cell variation (Fig. 13). In the subsequent cycles, the nucleation overpotentials of all discharge-voltage-limited cells become comparable, regardless of pre-lithiation. However, differences in the shape of the voltage profiles remain evident. The pre-lithiated electrodes exhibit a sharp, nearly vertical voltage drop at the onset of nucleation, whereas the non-pre-lithiated electrodes show a more gradual, sloping decrease, particularly for the cells limited to 0.57 and 0.45 V (compare Figs. 13 and S10).

A comparison of CE and stripping capacity for the Sn@Cu Li cell at an upper cut-off voltage of 0.57 V (blue), alongside the Cu Li cell (orange), is shown in Figure S18 (Supplementary Information). Although the bare Cu Li cell initially shows a higher stripping capacity (likely due to Sn alloy lithiation and Sn oxide reduction in Sn@Cu, which lead to a larger initial irreversible capacity in Sn@Cu), it rapidly declines within the first 25 cycles to much lower values, then stabilises for ~75 cycles before failure. This comparison highlights both the potential of Sn seed layers—particularly pre-lithiated Sn under restricted discharge—and the limitations of half-cells, where the large Li reservoir masks degradation from active material loss. Accordingly, this work focuses on interfacial electrochemical properties rather than overall half-cell performance.

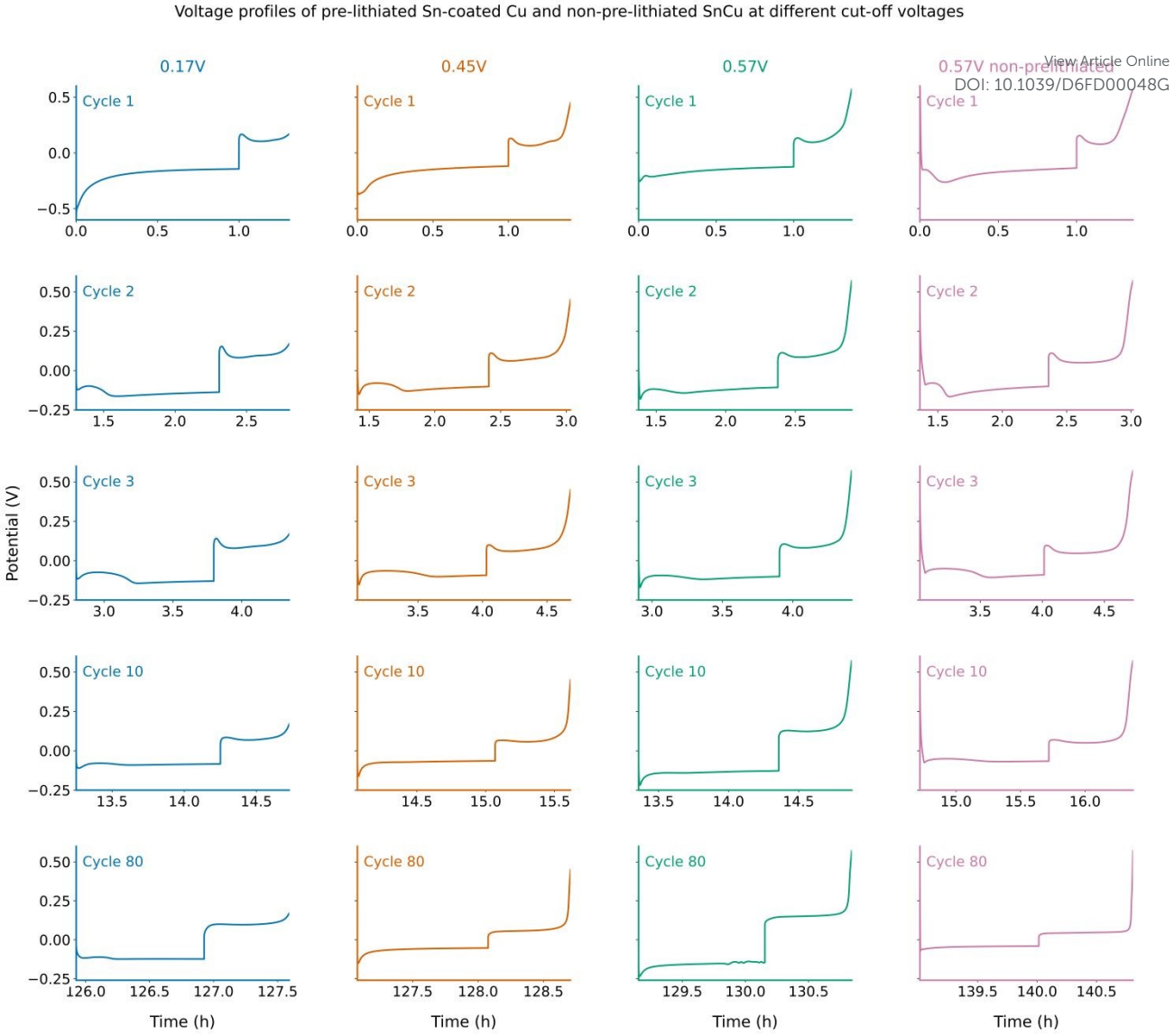

Figure 13 Voltage profiles of the pre-lithiated Sn(1 h)@Cu sample cycled with cut-off voltage at 0.17 V (blue), 0.45 V (orange), and 0.57 V (green). Voltage profiles of non-pre-lithiated Sn(1 h)@Cu sample cycled with cut-off voltage at 0.57 V (pink) were also included as a comparison. All the cells were cycling at 0.5 mA cm^{-2} with the capacity of 0.5 mAh cm^{-2}.

5. Investigation of the Sn/Cu-electrolyte interface

To investigate the evolution of charge transport across the Cu–electrolyte and Sn@Cu–electrolyte interfaces, SECM approach-curve measurements were performed using Fc^+/Fc as the redox mediator. As shown in Fig. 14a, both the bare Cu and Sn@Cu electrodes exhibit negative feedback, evidenced by the decrease in normalized tip current as the tip approached the substrate. This behaviour indicates that mediator regeneration at the substrate is hindered relative to diffusion in bulk solution, consistent with the presence of partially blocking interfacial layer and finite heterogeneous electron-transfer kinetics.

The approach curves for both electrodes suggest that the surfaces are partially blocked by an oxide or passivation layer (Fig. 14). For the Cu@Sn substrate, the approach curve lies slightly higher than that of bare Cu, indicating a lower degree of blocking and somewhat more facile interfacial charge transfer. This may arise because, although Cu is intrinsically more conductive than Sn@Cu,[31,32] its surface passivates more rapidly upon exposure to the electrolyte. The passivation behaviour observed for bare Cu is consistent with the formation of a native SEI (N-SEI) on Cu in $LiPF_6$–carbonate electrolytes, as previously reported by Menkin *et al.* [23] This interphase, typically containing LiF, copper

oxides and other electrolyte decomposition products, is thought to be thin and spatially heterogeneous, permitting limited—but not fully unhindered—electron transfer across the interface. [23]

View Article Online
DOI: 10.1039/D6FD00048G

When the Sn@Cu substrate was biased at + 0.57 V, the SECM approach curve exhibited stronger negative feedback compared to Sn@Cu at OCP, indicating limited regeneration of the Fc^+/Fc mediator at the substrate surface and therefore slower heterogeneous electron-transfer kinetics. At + 0.45 V, the curve shifted upward, indicating weaker negative feedback and enhanced mediator regeneration. A further increase in interfacial activity was observed at + 0.17 V, where the extracted kinetic parameters reached their maximum values (Fig 14c), suggesting the most favourable charge-transfer conditions at this potential. In contrast, at + 0.005 V, the approach curve shifted downward again, corresponding to stronger negative feedback and slower interfacial kinetics. This behaviour may be associated with increased surface blocking due to excessive SEI and possibly Li underpotential deposition on the Sn@Cu surface. Overall, the results demonstrate that the charge-transfer properties of the Sn@Cu interface are strongly potential dependent in LP57, with the highest activity observed at intermediate potentials (+ 0.17 to + 0.45 V).

Beyond the qualitative interpretation of the approach curves, the experimental data were analysed using established SECM theory to extract the dimensionless effective kinetic parameter κ, which describes the ratio between the heterogeneous reaction rate at the substrate and the diffusion rate of the mediator.[19] The corresponding heterogeneous electron-transfer rate constant k^0 was calculated using the Eq. 2.

$$(2) \quad k^0 = \frac{\kappa D}{a}$$

where D is the diffusion coefficient of the mediator, D = 1.5 x 10^{-3} cm s^{-1}, [33] and a is the radius of the ultramicroelectrode tip, 5 x 10^{-4} cm.

The bare Cu substrate exhibits a relatively low kinetic parameter (κ = 0.23) and electron-transfer rate constant (k^o = 6.9 × 10^{-3} cm s^{-1}), indicating moderate kinetics and significant interfacial blocking due to the formation of the N-SEI. This behaviour is consistent with a partially passivating native interphase formed in $LiPF_6$-based carbonate electrolyte, which hinders but does not fully suppress interfacial charge transfer.[23] In contrast, the Sn-coated Cu electrode exhibits higher κ (0.24–0.35) and k^o (7.1–10.5 × 10^{-3} cm s^{-1}) values across the investigated potentials, confirming enhanced interfacial electron-transfer kinetics compared with bare Cu. This indicates that the Sn coating modifies the interfacial structure, leading to reduced passivation and more efficient mediator regeneration.[34,35] The similar trend was observed for another Sn@Cu sample when applied potential of + 0.57 V, + 0.45 V and +0.17 V as shown in Fig S17. The summary of the derived κ and k^0 are summarized in Table S3.

While these SECM-derived kinetic parameters clearly demonstrate improved interfacial charge-transfer behaviour for Sn@Cu relative to bare Cu, the absence of directly comparable electrochemical cycling data; particularly Coulombic efficiency and long-term cycling performance for the bare Cu electrode limits a direct correlation between local interfacial kinetics and macroscopic electrochemical behaviour. As such, although the enhanced κ and k^o values strongly suggest that Sn coating facilitates improved charge transport and reduced interfacial blocking, caution must be exercised in linking these findings quantitatively to practical battery performance.

Overall, the SECM results indicate that Sn coating significantly alters the interfacial electrochemical reactivity of Cu, promoting faster electron-transfer kinetics and reduced passivation, particularly at intermediate potentials. However, a comprehensive understanding of how these local kinetic enhancements translate into improved cycling stability and efficiency requires systematic comparison with bare Cu under

identical electrochemical cycling conditions. Future work combining SECM analysis with galvanostatic cycling and Coulombic efficiency measurements will be essential to establish a direct structure–property–performance relationship for these electrode systems.

View Article Online
DOI: 10.1039/D6FD00048G

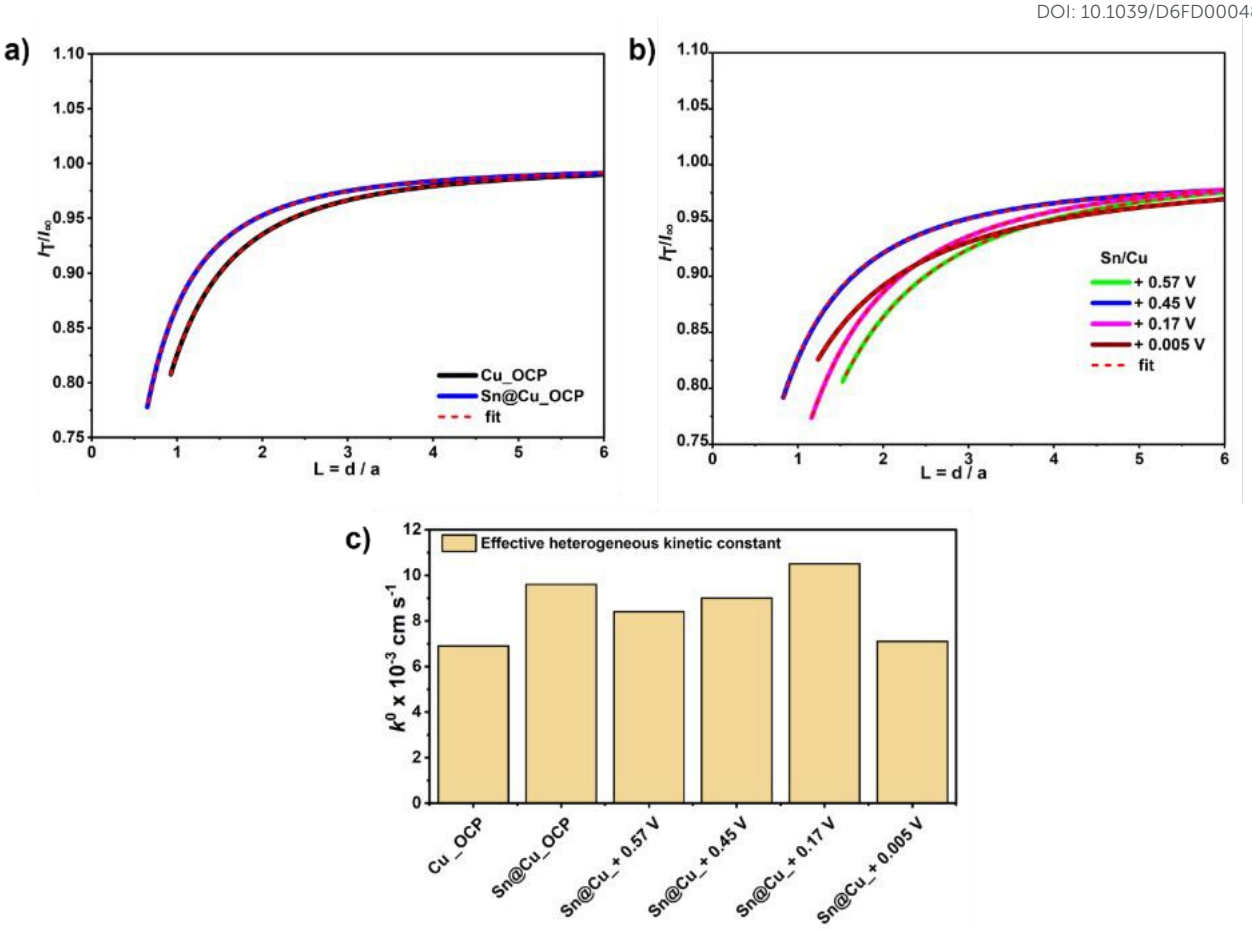

Figure 14 SECM feedback approach curves and extracted kinetic parameters for Cu and Sn@Cu electrodes. (a) Normalized SECM approach curves recorded above a Cu substrate at and Sn@Cu electrodes at OCP in 0.005 M ferrocene mediator dissolved in 1 M LP57 electrolyte. The experimental data (solid lines) are compared with theoretical fits (red dashed lines) based on the model of Cornut and Lefrou. The approach curves are plotted as a function of the normalized distance L=d/a, where dis the tip–substrate separation and ais the radius of the Pt UME. (b) Normalized SECM approach curves obtained for the Sn@Cu electrode at different applied potentials (+0.57 V, +0.45 V, +0.17 V, and +0.005 V). Red dashed lines represent theoretical fits used to extract kinetic parameters. (c) Bar diagram of the effective heterogeneous kinetics constant (k^0) values for Cu at OCP and Sn@Cu at OCP, (+0.57 V, +0.45 V, +0.17 V, 0.005 V) derived from fitting the experimental approach curves. Values of k^0 reported in units of x 10^{-3} cm s^{-1}.

Discussion

Immersion Sn plating resulted in the formation of a homogeneous and conformal Cu_6Sn_5 intermetallic coating that retained its overall composition during prolonged storage. XRD and EDX analyses (Figs. 1–2 and Fig. S2 in the SI) confirmed that the coating consists of Cu_6Sn_5 intermetallic phases together with residual metallic Sn. Nevertheless, ongoing solid-state interdiffusion in the Cu–Sn system promotes continuous growth and redistribution within the intermetallic layer, leading to gradual thickening of the coating and possible exposure of additional electrochemically active Sn at the surface. Furthermore, partial oxidation of surface Sn during storage results in increased Sn oxide reduction in the initial cycles, contributing to a higher apparent capacity and variations in anode performance upon storage (Figs. 6-8).[36]

The overpotentials associated with Li–Sn alloying in the Sn@Cu electrode were observed in the potential range of 0.25–0 V vs. Li^+/Li during lithiation in the first few cycles, and 0.6–0.8 V vs. Li^+/Li during de-lithiation (Figs. 4-7). These values are in reasonable agreement with previously reported overpotentials of 0.57, 0.45, and 0.17 V vs. Li^+/Li for Sn anodes.[37] Notably, no distinct alloying features were observed in the 0.6–0.8 V region during lithiation, either in cyclic voltammetry or under galvanostatic conditions.

This absence is likely related to additional polarization contributions arising from the reduction of native surface SnO_x species and the concurrent formation of the SEI, which can broaden or mask the intrinsic alloying response.

View Article Online
DOI: 10.1039/D6FD00048G

Cycling of Sn@Cu vs. Li cells revealed an initial increase in capacity during the first 2–5 cycles, which is attributed to progressive SEI formation and the electrochemical reduction of native Sn oxides (Fig.7-8). A continuous capacity decrease is observed throughout cycles 5–45, consistent with the larger alloying contribution. At later stages of cycling Li stripping becomes the dominant contributor to the discharge capacity. During this regime, the capacity exhibits a characteristic increase followed by a decrease, forming a distinct “capacity peak”. This behaviour is attributed to the temporary stabilisation of a newly formed Sn-degraded interface, followed by progressive degradation of the freshly formed Li metal anode. Finally, significant capacity oscillations in the discharge capacity measured during the cycles following cycle 70 were attributed to cell failure.

When lower cut-off potentials (0.57, 0.45, or 0.17 V vs. Li/Li^+) were applied during discharge, the characteristic alloying voltage signature was no longer observed beyond the first cycle (Fig. S9). The corresponding capacity peaks disappeared (Fig. 10). The cells exhibited distinct cycling behaviours depending on the selected cut-off voltage. At a cut-off potential of 0.57 V, the capacity initially increased before gradually declining with continued cycling. In contrast, at lower cut-off potentials 0.45 and 0.17 V, the capacity showed a slow but continuous decay over approximately 100 cycles. This behaviour is likely related to differences in the extent of de-alloying and Li stripping. At 0.57 V, only partial de-alloying may occur, which can accelerate structural degradation and capacity fading. Conversely, a cut-off potential of 0.17 V may be insufficient to enable complete Li stripping, leading to the accumulation of inactive Li and progressive capacity loss. Therefore, a cut-off potential of 0.45 V appears to provide a more favourable balance between effective Li stripping and structural stability.

The evolution of Sn capacity is governed by two competing mechanisms. Increased exposure of electrochemically active Sn enhances capacity by enlarging the accessible surface area. However, the same surface area increase accelerates degradation through sustained SEI growth and the formation of electrically isolated (“dead”) Sn arising from alloy cracking and loss of electronic connectivity during cycling. As a result, the measured capacity represents the net effect of these opposing contributions. Limiting the lower discharge cut-off voltage reduces the extent of Sn de-alloying, thereby mitigating structural degradation and leading to higher reversible capacity and more stable long-term cycling.

Chemical pre-lithiation markedly improved the cycling behaviour of Sn@Cu electrodes, enabling higher capacity and longer cycle life compared to voltage-limited cells without pre-lithiation. Chemical pre-lithiation enables gradual lithiation and SEI formation prior to electrochemical cycling. Consequently, less capacity is required for SEI formation, resulting in higher reversible capacity and improved long-term stability. Moreover, the improved cycling stability is attributed to the reduced extent of repeated Sn alloying/de-alloying during subsequent cycling, as evidenced by the absence of pronounced Sn layer cracking in SEM images of stripped electrodes (Fig. 11). The suppressed alloying activity is likely a consequence of the initially deeper lithiation achieved during prolonged chemical pre-lithiation, which modifies the subsequent electrochemical reaction pathway.

Our findings highlight the pivotal role of SEI formation in governing Li metal reversibility. Although a fraction of the initial capacity is consumed during SEI growth, lithiation of the Sn interlayer promotes the development of a more kinetically favourable interphase. Using SECM, we directly demonstrate enhanced interfacial charge-transfer kinetics at lithiated Sn surfaces. Faster interfacial kinetics potentially result in reduced local kinetic heterogeneity, which in turn mitigates current hot spots and suppresses unstable Li nucleation, enabling dense, dendrite-free Li electrodeposition. Consequently, more uniform interfacial reaction pathways facilitate efficient Li stripping and significantly limit the formation of dead Li. These results underline the power of SECM as a uniquely sensitive tool for probing local SEI transport properties and linking interfacial kinetics to macroscopic cycling stability.

These results demonstrate that metal–metal wetting in electrochemical systems cannot be reliably inferred from the commonly used nucleation overpotential. The measured nucleation voltage represents a convolution of multiple processes, including ionic transport limitations, interfacial charge-transfer kinetics, SEI resistance, surface heterogeneity, and evolving reaction pathways such as alloy formation. Consequently, similar nucleation overpotentials may correspond to markedly different deposition morphologies and interfacial stability. In reactive host materials, wetting is instead governed by the dynamic evolution of interfacial energetics, chemo-mechanical stresses, and mass transport during cycling. Therefore, direct evaluation of deposition uniformity and interfacial structural evolution provides a more meaningful descriptor of effective metal wetting and long-term electrode performance, as demonstrated here. These findings call for a reassessment of nucleation overpotential as a primary optimisation metric for metal anodes. Overall, the results establish Sn-based interlayers as a promising strategy for stabilising Li deposition behaviour, offering a practical route towards improving the reliability and lifetime of anode-free Li metal batteries.

Conclusions

View Article Online
DOI: 10.1039/D6FD00048G

Immersion Sn plating enables the formation of a conformal Cu_6Sn_5 intermetallic host that supports reversible Li storage in anode-free configurations, highlighting the potential of Sn coatings for stabilising Li metal anodes. The electrochemical behaviour of Sn@Cu electrodes is governed by the coupled evolution of Sn–Li alloying, Li deposition/stripping, and SEI growth, with capacity determined by the balance between increased accessibility of active Sn and progressive interfacial degradation. Limiting the lower discharge cut-off voltage suppresses excessive de-alloying and improves cycling stability, while chemical pre-lithiation further enhances performance by promoting controlled interphase formation and mitigating alloying-induced damage. Importantly, nucleation overpotential is shown to be an insufficient descriptor of metal wetting, whereas SECM enables direct evaluation of local SEI evolution and deposition uniformity. Further optimisation of the Sn coating thickness and translation of these strategies to full-cell architectures are expected to improve formation efficiency, stabilise Li inventory, and enable higher energy density and longer cycle life in anode-free batteries.

Data availability

The data supporting this article have been included as part of the ESI. Details on the tin coating procedure, EDX spectra and data, additional CV and cycling plots, additional SEM images. Data for this article are available at Apollo – University of Cambridge Repository at ID: D0BAE1BA-2D13-4BC1-BBD4-5251F35335B0.

Author contributions

Conceptualization, Resources and Project administration: S.M. Supervision: S.M.; day-to-day supervision: X.S., E.W. Methodology: S.M., X.S., K.P., E.W., R.N. Investigation: X.S., R.N., E.W., K.P., V.S. Formal analysis: X.S., R.N., K.P. Writing – original draft: X.S., R.N., K.P., S.M. Review and editing: All authors.

Conflicts of interest

There are no conflicts to declare.

Acknowledgements

SM, EW and XS gratefully acknowledge funding by the Royal Society University Research Fellowship (URF, URF\R1\231513), Research Grants 2024 [RGS\R2\242207], Faraday Institution DEGRADATION project FIRG024 and Faraday Institution PhD Enrichment Scheme. KP and SM gratefully acknowledge funding by Faraday Institution SAFEBATT project FIRG028 and the Issac Newton Trust (INT) G582256

Notes and references

(1) Menkin, S.; Ayerbe, E.; Gunnarsdóttir, A. B.; Del Olmo, D.; López-Aranguren, P.; Rafique, A.; Rikarte, J.; Chauque, S.; Shi, X.; Guillon, O.; Dominko, R.; Schlee, P.; Finsterbusch, M.; Kvasha, A.; Fattakhova-Rohlfing, D. Anode-Free Cell Concepts: Critical Analysis and Development of Practical Batteries. *Small* **2026**, e13633. https://doi.org/10.1002/smll.202513633.

(2) Wu, L.; Pei, F.; Zhang, Y.; Long, Z.; Liao, Y.; Lv, W.; Li, Y.; Zhang, W.; Xu, H.; Huang, Y. LiI-Coated Li-Sn Alloy Composite Anode for Lithium Metal Batteries with Solid Polymer Electrolyte. *ACS Energy Lett.* **2024**, *9* (12), 5992–6001. https://doi.org/10.1021/acsenergylett.4c02615.

(3) Menkin, S.; Golodnitsky, D.; Peled, E. Artificial Solid-Electrolyte Interphase (SEI) for Improved Cycleability and Safety of Lithium–Ion Cells for EV Applications. *Electrochemistry Communications* **2009**, *11* (9), 1789–1791. https://doi.org/10.1016/j.elecom.2009.07.019.

(4) Yan, K.; Lu, Z.; Lee, H.-W.; Xiong, F.; Hsu, P.-C.; Li, Y.; Zhao, J.; Chu, S.; Cui, Y. Selective Deposition and Stable Encapsulation of Lithium through Heterogeneous Seeded Growth. *Nat Energy* **2016**, *1* (3), 16010. https://doi.org/10.1038/nenergy.2016.10.

(5) Li, N.; Yin, Y.; Yang, C.; Guo, Y. An Artificial Solid Electrolyte Interphase Layer for Stable Lithium Metal Anodes. *Advanced Materials* **2016**, *28* (9), 1853–1858. https://doi.org/10.1002/adma.201504526.

(6) Zhang, Z.; Luo, H.; Liu, Z.; Wang, S.; Zhou, X.; Liu, Z. A Chemical Lithiation Induced $Li_{4.4}$ Sn Lithiophilic Layer for Anode-Free Lithium Metal Batteries. *J. Mater. Chem. A* **2022**, *10* (17), 9670–9679. https://doi.org/10.1039/D2TA00167E.

(7) Yan, K.; Lu, Z.; Lee, H.-W.; Xiong, F.; Hsu, P.-C.; Li, Y.; Zhao, J.; Chu, S.; Cui, Y. Selective Deposition and Stable Encapsulation of Lithium through Heterogeneous Seeded Growth. *Nat Energy* **2016**, *1* (3), 16010. https://doi.org/10.1038/nenergy.2016.10.

(8) Wang, X.; He, Y.; Tu, S.; Fu, L.; Chen, Z.; Liu, S.; Cai, Z.; Wang, L.; He, X.; Sun, Y. Li Plating on Alloy with Superior Electro-Mechanical Stability for High Energy Density Anode-Free Batteries. *Energy Storage Materials* **2022**, *49*, 135–143. https://doi.org/10.1016/j.ensm.2022.04.009.

(9) Hawari, N. H.; Huang, X.; Butarbutar, L. M.; Prayogi, A.; Hidayat, H. N.; Sumboja, A.; Ding, N. Unveiling the Effect of Alloy-Type Coating for Lithium Metal Plating and Stripping on Anode-Free Lithium Metal Batteries. *Journal of Alloys and Compounds* **2024**, *975*, 172988. https://doi.org/10.1016/j.jallcom.2023.172988.

(10) Ko, D.-S.; Kim, S.; Lee, S.; Yoon, G.; Kim, D.; Shin, C.; Kim, D.; Lee, J.; Sul, S.; Yun, D.-J.; Jung, C. Mechanism of Stable Lithium Plating and Stripping in a Metal-Interlayer-Inserted Anode-Less Solid-State Lithium Metal Battery. *Nat Commun* **2025**, *16* (1), 1066. https://doi.org/10.1038/s41467-025-55821-1.

(11) Zhang, S. S.; Fan, X.; Wang, C. A Tin-Plated Copper Substrate for Efficient Cycling of Lithium Metal in an Anode-Free Rechargeable Lithium Battery. *Electrochimica Acta* **2017**, *258*, 1201–1207. https://doi.org/10.1016/j.electacta.2017.11.175.

(12) Molaiyan, P.; Abdollahifar, M.; Boz, B.; Beutl, A.; Krammer, M.; Zhang, N.; Tron, A.; Romio, M.; Ricci, M.; Adelung, R.; Kwade, A.; Lassi, U.; Paolella, A. Optimizing Current Collector Interfaces for Efficient "Anode-Free" Lithium Metal Batteries. *Adv Funct Materials* **2024**, *34* (6), 2311301. https://doi.org/10.1002/adfm.202311301.

(13) Zhang, S. S.; Fan, X.; Wang, C. A Tin-Plated Copper Substrate for Efficient Cycling of Lithium Metal in an Anode-Free Rechargeable Lithium Battery. *Electrochimica Acta* **2017**, *258*, 1201–1207. https://doi.org/10.1016/j.electacta.2017.11.175.

(14) Huttunen-Saarivirta, E.; Tiainen, T. Autocatalytic Tin Plating in the Fabrication of Tin-Coated Copper Tube. *Journal of Materials Processing Technology* **2005**, *170* (1–2), 211–219. https://doi.org/10.1016/j.jmatprotec.2005.04.113.

(15) Study of Immersion Tin Plating for the Production of Printed Circuit Boards. *Int. J. Corros. Scale Inhib.* **2023**, *12* (4). https://doi.org/10.17675/2305-6894-2023-12-4-17.

(16) Study of Immersion Tin Plating for the Production of Printed Circuit Boards. *Int. J. Corros. Scale Inhib.* **2023**, *12* (4). https://doi.org/10.17675/2305-6894-2023-12-4-17.

(17) Wang, X.; He, Y.; Tu, S.; Fu, L.; Chen, Z.; Liu, S.; Cai, Z.; Wang, L.; He, X.; Sun, Y. Li Plating on Alloy with Superior Electro-Mechanical Stability for High Energy Density Anode-Free Batteries. *Energy Storage Materials* **2022**, *49*, 135–143. https://doi.org/10.1016/j.ensm.2022.04.009.

(18) Fei, X.; Gao, H.; Xu, Y.; Ma, W.; Yu, B.; Tan, F.; Cheng, G.; Zhang, Z. Porous Lithiophilic Cu-Sn Solid Solution Current Collector for Dendrite-Free Lithium Metal Batteries. *Energy Storage Materials* **2024**, *65*, 103079. https://doi.org/10.1016/j.ensm.2023.103079.

(19) Cornut, R.; Lefrou, C. New Analytical Approximation of Feedback Approach Curves with a Microdisk SECM Tip and Irreversible Kinetic Reaction at the Substrate. *Journal of Electroanalytical Chemistry* **2008**, *621* (2), 178–184. https://doi.org/10.1016/j.jelechem.2007.09.021.

(20) Arra, M. Aging Mechanisms of Immersion Tin and Silver PCB Surface Finishes in Lead-Free Solder Applications; IPC, 2003.

(21) Chen, Y.-H.; Wang, Y.-Y.; Wan, C.-C. Microstructural Characteristics of Immersion Tin Coatings on Copper Circuitries in Circuit Boards. *Surface and Coatings Technology* **2007**, *202* (3), 417–424. https://doi.org/10.1016/j.surfcoat.2007.06.004.

(22) Courtney, I. A.; Dahn, J. R. Electrochemical and In Situ X-Ray Diffraction Studies of the Reaction of Lithium with Tin Oxide Composites. *J. Electrochem. Soc.* **1997**, *144* (6), 2045–2052. https://doi.org/10.1149/1.1837740.

(23) Menkin, S.; O'Keefe, C. A.; Gunnarsdóttir, A. B.; Dey, S.; Pesci, F. M.; Shen, Z.; Aguadero, A.; Grey, C. P. Toward an Understanding of SEI Formation and Lithium Plating on Copper in Anode-Free Batteries. *J. Phys. Chem. C* **2021**, *125* (30), 16719–16732. https://doi.org/10.1021/acs.jpcc.1c03877.

(24) Park, C.; Kim, J.; Lim, W.; Lee, J. Toward Maximum Energy Density Enabled by Anode-free Lithium Metal Batteries: Recent Progress and Perspective. *Exploration* **2024**, *4* (2), 20210255. https://doi.org/10.1002/EXP.20210255.

(25) Wan, M.; Kang, S.; Wang, L.; Lee, H.-W.; Zheng, G. W.; Cui, Y.; Sun, Y. Mechanical Rolling Formation of Interpenetrated Lithium Metal/Lithium Tin Alloy Foil for Ultrahigh-Rate Battery Anode. *Nat Commun* **2020**, *11* (1), 829. https://doi.org/10.1038/s41467-020-14550-3.

(26) Frerichs, J. E.; Ruttert, M.; Böckmann, S.; Winter, M.; Placke, T.; Hansen, M. R. Identification of Li_xSn Phase Transitions During Lithiation of Tin Nanoparticle-Based Negative Electrodes from Ex Situ^{119}Sn MAS NMR and Operando^{7}Li NMR and XRD. *ACS Appl. Energy Mater.* **2021**, *4* (7), 7278–7287. https://doi.org/10.1021/acsaem.1c01405.

(27) Jeon, Y.; Lee, D. J.; Zheng, H.; Behara, S. S.; Lee, J.-P.; Wu, J.; Li, F.; Tang, W.; Zhang, L.; Chen, Y.-T.; Xu, D.; Kim, J.; Song, M.-S.; Van Der Ven, A.; He, K.; Chen, Z. Lithium Diffusion-Controlled Li-Al Alloy Negative Electrode for All-Solid-State Battery. *Nat Commun* **2025**, *16* (1), 9629. https://doi.org/10.1038/s41467-025-64386-y.

(28) Jia, W.; Zhang, J.; Zheng, L.; Zhou, H.; Zou, W.; Wang, L. Lithium-Rich Alloy as Stable Lithium Metal Composite Anode for Lithium Batteries. *eScience* **2024**, *4* (6), 100266. https://doi.org/10.1016/j.esci.2024.100266.

(29) Amardeep, A.; Freschi, D. J.; Wang, J.; Liu, J. Fundamentals, Preparation, and Mechanism Understanding of Li/Na/Mg-Sn Alloy Anodes for Liquid and Solid-State Lithium Batteries and Beyond. *Nano Res.* **2023**, *16* (6), 8191–8218. https://doi.org/10.1007/s12274-023-5448-x.

(30) Obrovac, M. N.; Chevrier, V. L. Alloy Negative Electrodes for Li-Ion Batteries. *Chem. Rev.* **2014**, *114* (23), 11444–11502. https://doi.org/10.1021/cr500207g.

(31) Kawaguchi, T.; Shimada, K.; Ichitsubo, T.; Yagi, S.; Matsubara, E. Surface-Layer Formation by Reductive Decomposition of LiPF6 at Relatively High Potentials on Negative Electrodes in Lithium Ion Batteries and Its Suppression. *Journal of Power Sources* **2014**, *271*, 431–436. https://doi.org/10.1016/j.jpowsour.2014.08.010.

(32) Stich, M.; Leppin, C.; Krauss, F. T.; Valdes Landa, J. E.; Pantenburg, I.; Roling, B.; Bund, A. Comparing the SEI Formation on Copper and Amorphous Carbon: A Study with Combined Operando Methods. *Batteries* **2025**, *11* (7), 273. https://doi.org/10.3390/batteries11070273.

(33) Wang, Y.; Rogers, E. I.; Compton, R. G. The Measurement of the Diffusion Coefficients of Ferrocene and Ferrocenium and Their Temperature Dependence in Acetonitrile Using Double Potential Step Microdisk Electrode Chronoamperometry. *Journal of Electroanalytical Chemistry* **2010**, *648* (1), 15–19. https://doi.org/10.1016/j.jelechem.2010.07.006.

(34) Guan, R.; Liu, S.; Wang, C.; Yang, Y.; Lu, D.; Bian, X. Lithiophilic Sn Sites on 3D Cu Current Collector Induced Uniform Lithium Plating/Stripping. *Chemical Engineering Journal* **2021**, *425*, 130177. https://doi.org/10.1016/j.cej.2021.130177.

(35) Ye, L.; Zhang, C.; Zhou, Y.; Ülgüt, B.; Zhao, Y.; Qian, J. Guided Lithium Nucleation and Growth on Lithiophilic Tin-Decorated Copper Substrate. *Journal of Energy Chemistry* **2022**, *74*, 412–419. https://doi.org/10.1016/j.jechem.2022.07.027.

(36) Laurila, T.; Vuorinen, V.; Kivilahti, J. K. Interfacial Reactions between Lead-Free Solders and Common Base Materials. *Materials Science and Engineering: R: Reports* **2005**, *49* (1–2), 1–60. https://doi.org/10.1016/j.mser.2005.03.001.

(37) Böhme, S.; Edström, K.; Nyholm, L. On the Electrochemistry of Tin Oxide Coated Tin Electrodes in Lithium-Ion Batteries. *Electrochimica Acta* **2015**, *179*, 482–494. https://doi.org/10.1016/j.electacta.2015.02.150.

View Article Online
DOI: 10.1039/D6FD00048G

Data availability

The data supporting this article have been included as part of the ESI. Details on the tin coating procedure, EDX spectra and data, additional CV and cycling plots, additional SEM images. Data for this article are available at Apollo – University of Cambridge Repository at ID: D0BAE1BA-2D13-4BC1-BBD4-5251F35335B0.